Schweizerischer Erdbebendienst
Service Sismologique Suisse
Servizio Sismico Svizzero
Swiss Seismological Service

ETH zürich

Riehen - Zur Hoffnung (SRHH)

SITE CHARACTERIZATION REPORT

Clotaire MICHEL, Manuel HOBIGER, Carlo CAUZZI

Valerio POGGI, Jan BURJANEK, Donat FÄH

Sonneggstrasse 5 CH-8092 Zürich Switzerland; E-mail: clotaire.michel@sed.ethz.ch

Last modified : January 5, 2015

Abstract

Ambient vibration array measurements were performed to characterize the site Riehen Zur Hoffnung. The site, where the new station SRHH of the Swiss Strong Motion Network was installed, is located on Loess hill at the edge of the Rhine graben in the North of Basel. The new station was installed in the frame of the Basel Erdbebenvorsorge project. In order to characterize the velocity profile under the station, array measurements with a $220\,\mathrm{m}$ aperture were performed. The measurements were successful and allowed deriving a velocity model for this site. The soil column underlying station SRHH station is made of a layer of Loess of 10 to $15\,\mathrm{m}$ depth with a velocity of 150 to $500\,\mathrm{m/s}$. The velocity contrast is clear with a layer at 1000 to $1300\,\mathrm{m/s}$, extending down to 90 to $120\,\mathrm{m}$ depth. Below the bedrock is found with a velocity of about $2000\,\mathrm{m/s}$.
$V_{s,30}$ is $534\,\mathrm{m/s}$ and the ground type in the Eurocode 8 [CEN, 2004] and the SIA261 [SIA, 2003] is E. The theoretical 1D SH transfer function and impedance contrast of the quarter-wavelength velocity computed from the inverted profiles show a large amplification at high frequency. The sedimentary layer is creating a resonance peak around $6-7\,\mathrm{Hz}$, whereas the contrast in the rock is creating a small peak at about $3\,\mathrm{Hz}$, corresponding to the "fundamental" peak from the H/V ratios.

Contents

1 Introduction

The station SRHH (Riehen - Zur Hoffnung) is part of the dense array of the Swiss Strong Motion Network (SSMNet) in Basel. SRHH has been installed in the framework of the Basel Erdbebenvorsorge project in 2013 as a new station. This project includes also the site characterization. Passive array measurements have been selected as a standard tool to investigate these sites. An array measurement campaign was carried out on 5th March 2014 in the area of the special school Zur Hoffnung (Fig. 1), with a centre close to SRHH, in order to characterize the velocity profile under this station. This station is located on a Loess hill at the edge of the Rhine graben. This report presents the measurement setup, the results of the H/V analysis and of the array processing of the surface waves (dispersion curves). Then, an inversion of these results into velocity profiles is performed. Standard parameters are derived to evaluate the amplification at this site.

Canton	City	Location	Station code	Site type	Slope
Basel Stadt	Riehen	Zur Hoffnung	SRHH	Loess hill	Slight slope

Table 1: Main characteristics of the study-site.

Figure 1: Picture of the site.

2 Geology

The geological map (Fig. 2) indicates that the site located on Loess hill from the Pleistocene. The region is heavily affected by NNE-SSW faulting of the eastern edge of the Rhine Graben. The geological map indicates nearby, in the same compartment, an outcrop of marls from lower Bajocian age (between the Blagdeni and the Murchisonae layers, Mesozoic) that would indicate that the quaternary sediments are approximately $10\,\mathrm{m}$ thick at the centre of the array, an possibly up to $25\,\mathrm{m}$ at the top of this hill. According to the map, the station RHH304 could be in a more interior compartment of the graben, whereas station RHH402 could be in a more exterior compartment as the rest of the array measurement. In the more exterior compartment, boreholes indicate a depth of $14\,\mathrm{m}$ of quaternary sediments on Trias (Keuper) marls or gypsum. Moreover, some stations of the inner rings (in the slope) may lay on weathered Loess.

According to the microzonation of Basel [Fäh and Huggenberger, 2006], the station is located in the zone Flexur-Nord, on Loess. In this zone, the microzonation is predicting a peak amplification of a factor of 3 in response spectrum at about $5\,\mathrm{Hz}$.

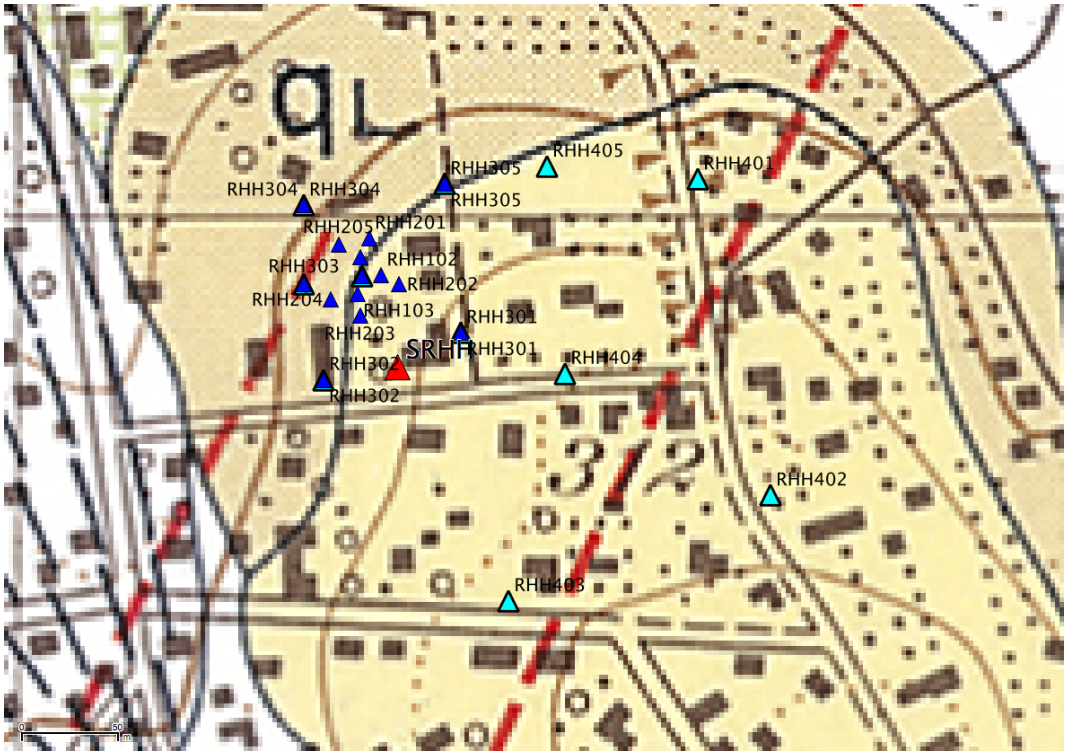

Figure 2: Geology and topography of the area, see Fig. 3 for the symbols concerning the array. Caption of the geological map, white: alluvia, yellow (major part of the zone): Loess, dark yellow (qL area in the North): weathered Loess, green crosshatching (North-West area): alluvial terrace, dashed red lines: supposed normal faults from the graben (dipping to the NW).

3 Experiment description

3.1 Ambient Vibrations

The ground surface is permanently subjected to ambient vibrations due to:

- natural sources (ocean and large-scale atmospheric phenomena) below $1\,\mathrm{Hz}$,
- local meteorological conditions (wind and rain) at frequencies around $1\,\mathrm{Hz}$,
- human activities (industrial machines, traffic…) at frequencies above $1\,\mathrm{Hz}$ [Bonnefoy-Claudet et al., 2006].

The objective of the measurements is to record these ambient vibrations and to use their propagation properties to infer the underground structure. First, the polarization of the recorded waves (H/V ratio) is used to derive the resonance frequencies of the soil column. Second, the arrival time delays at many different stations are used to derive the velocity of surface waves at different frequencies (dispersion). The information (H/V, dispersion curves) is then used to derive the properties of the soil column using an inversion process.

3.2 Equipment

For these measurements 11 Quanterra Q330 dataloggers named NR02 to NR12 and 14 Lennartz 3C 5 s seismometers were available (see Tab. 2). Each datalogger can record on 2 ports A (channels EH1, EH2, EH3 for Z, N, E directions) and B (channels EH4, EH5, EH6 for Z, N, E directions). Time synchronization was ensured by GPS. The sensors were placed on a metal tripod, in a $20\,\mathrm{cm}$ deep hole, when necessary, for better coupling with the ground.

Digitizer	**Model**	**Number**	**Resolution**
	Quanterra Q330	11	$24\,\mathrm{bits}$
Sensor type	**Model**	**Number**	**Cut-off frequency**
Velocimeter	Lennartz 3C	14	$0.2\,\mathrm{Hz}$

Table 2: Equipment used.

3.3 Geometry of the arrays

Two array configurations were used. The first configuration is made of 3 rings of 10, 20 and $50\,\mathrm{m}$ radius around a central station for a total of 14 sensors; the second configuration includes the outer ring of the first configuration (plus the central station) and an array of 5 more sensor forming a ring of $110\,\mathrm{m}$ radius around the center of the hill (total of 11 sensors). The minimum inter-station distance and the aperture are therefore 10 and $100\,\mathrm{m}$ and 50 and $220\,\mathrm{m}$, respectively. The experimental setup is displayed in Fig. 3. The final usable datasets are detailed in section 4.2.

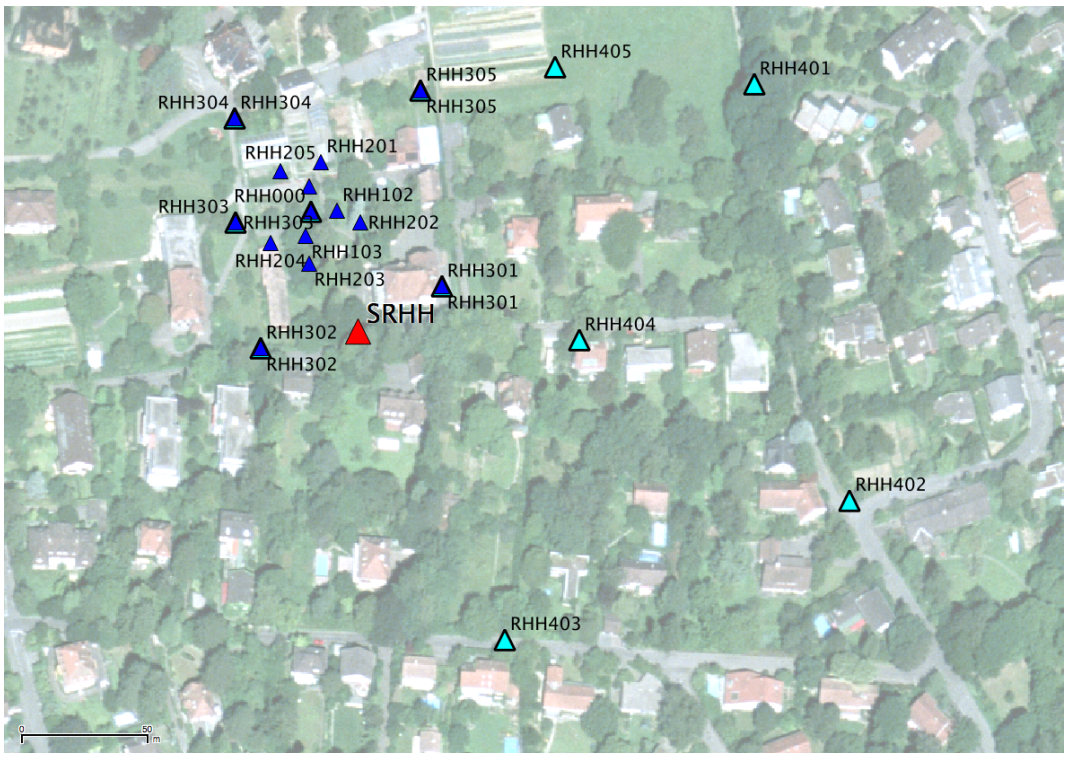

Figure 3: Geometry of the arrays. Deep blue triangles refer to the first configuration and triangles with thick edges refer to the second configuration.

3.4 Positioning of the stations

The sensor coordinates were measured using a differential GPS device (Leica Viva GS10), including only a rover station and using the Real Time Kinematic technique provided by Swisstopo. It allows an absolute positioning with an accuracy better than $5\,\mathrm{cm}$ on the Swissgrid. However, this accuracy was not reached at few points due to trees. The less accurate points were: RHH103 with $58\,\mathrm{cm}$ (anyway not used in the array analysis see next section), RHH401 with $21\,\mathrm{cm}$ and RHH203 with $19\,\mathrm{cm}$.

4 Data quality

4.1 Usable data

The largest time windows were extracted, for which all the sensors of the array were correctly placed and the GPS synchronization was ensured. Z component of sensor RHH103 did not work, probably because the cable was badly connected. A pin of a cable has been broken when connected to RHH403, so that N component did not work for this deployment. Recordings are generally consistent. Sensor RHH201 has been kicked once, higher noise at RHH305 during the second configuration and above 1Hz at RHH304 are noticed.

Orientations of the sensors were checked by maximizing the correlation with the central station at low frequencies [Poggi et al., 2012b]. Deviations lower than $6\,^\circ$ were found for all points. Original and rotated datasets are available for the 3C array analysis.

The characteristics of the datasets are detailed in Tab. 3.

4.2 Data processing

The data were first converted to SAC format including in the header the coordinates of the point (CH1903 system), the recording component and a name related to the position. The name is made of 3 letters characterizing the location (RHH here), 1 digit for the ring and 2 more digits for the number in the ring. Recordings were not corrected for the instrumental response.

Dataset	Starting Date	Time	Length	F_s	Min. inter-distance	Aperture	# of points
1	2014/03/05	10:46	123 min	200 Hz	10 m	100 m	13
2	2014/03/05	13:13	140 min	200 Hz	50 m	220 m	10

Table 3: Usable datasets.

5 H/V processing

5.1 Processing method and parameters

In order to process the H/V spectral ratios, several codes and methods were used. The classical H/V method was applied using the Geopsy `http://www.geopsy.org` software. In this method, the ratio of the smoothed Fourier Transform of selected time windows are averaged. Tukey windows (cosine taper of 5% width) of $50\,\mathrm{s}$ long overlapping by 50% were selected. Konno and Ohmachi [1998] smoothing procedure was used with a b value of 60. The classical method computed using the method of Fäh et al. [2001] was also performed.

Moreover, the time-frequency analysis method [Fäh et al., 2009] was used to estimate the ellipticity function more accurately using the Matlab code of V. Poggi. In this method, the time-frequency analysis using the Wavelet transform is computed for each component. For each frequency, the maxima over time (10 per minute with at least $0.1\,\mathrm{s}$ between each) in the TFA are determined. The Horizontal to Vertical ratio of amplitudes for each maximum is then computed and statistical properties for each frequency are derived. A Cosine wavelet with parameter 9 is used. The mean of the distribution for each frequency is stored. For the sake of comparison, the time-frequency analysis of Fäh et al. [2001], based on the spectrogram, was also used.

The ellipticity extraction using the Capon analysis [Poggi and Fäh, 2010] (see section on array analysis) was also performed.

Method	Freq. band	Win. length	Anti-trig.	Overlap	Smoothing
Standard H/V Geopsy	$0.2-20\,\mathrm{Hz}$	$50\,\mathrm{s}$	No	50%	K&O 60
Standard H/V D. Fäh	$0.2-20\,\mathrm{Hz}$	$30\,\mathrm{s}$	No	75%	-
H/V TFA D. Fäh	$0.2-20\,\mathrm{Hz}$	Specgram	No	-	-
H/V TFA V. Poggi	$0.2-20\,\mathrm{Hz}$	Cosine wpar=9	No	-	No

Table 4: Methods and parameters used for the H/V processing.

5.2 Results

The H/V curves are the same below 1Hz, but in general variable in the area (Fig. 4). They are relatively flat with an amplitude around 2.4. The low frequency behavior is complex and may be influenced by the Rhine graben. Uebayashi et al. [2012] showed that plateau-like H/V ratios were due to steps in the geology (faults) as at the border of the Rhine graben. The results for RHH202, different from all the other points at low frequency, are not trusted. Points 305, 401, 402, 404 and 405 show a peak additionally to the the other points between 2 and $2.3\,\mathrm{Hz}$ (increasing frequency to the East). The central zone of the array (points 000, 101, 102, 201, 203, 204, 205, 303) is also particular with a clear high frequency peak from 6 to $8.5\,\mathrm{Hz}$, increasing for stations up on the hill. Points 304 and 302 are somehow in-between these two behaviors (Fig. 5): They have the same low frequency behavior as the central stations without the clear high frequency peak (one layer less?). The interpretation would be a sequence of two layers. A shallow layer is present only in the central zone of the array is very variable. Below, another

layer exist at all other points that is deeper at points 404, 401, 402 etc than in the central part of the array.

In Fig. 7 the H/V ratios of the accelerometric station SRHH and the temporary station XBA33, located in the building nearby are presented. Several peaks with anthropic origin (especially at 1.15, 9.34, 11.3, 14 and $17.8\,\mathrm{Hz}$) disturb the H/V ratios. Though the accelerometeric station is not reliable at low frequency, they show the same values. They deviate above $8\,\mathrm{Hz}$ due to the filtering of the foundation of the building. Station SRHH has an intermediate behavior between point RHH302 and point RHH000: the shallower layer is presenting a peak above $9\,\mathrm{Hz}$ but is not clear. A low frequency peak, named later "fundamental" at the SRHH station is therefore at about $3 - 4\,\mathrm{Hz}$, with a peak amplitude around 2 for the TFA methods. Deeper resonances are however not excluded.

Moreover, all the methods to compute H/V ratios are compared at the array centre on Fig. 6, in which the classical methods were divided by $\sqrt{2}$ to correct from the Love wave contribution [Fäh et al., 2001]. The classical and TFA methods match well at high frequencies but large variations are observed at low frequencies. The 3C FK analysis from the first configuration (Capon method) is representative for the array centre, although the peak is smoothed.

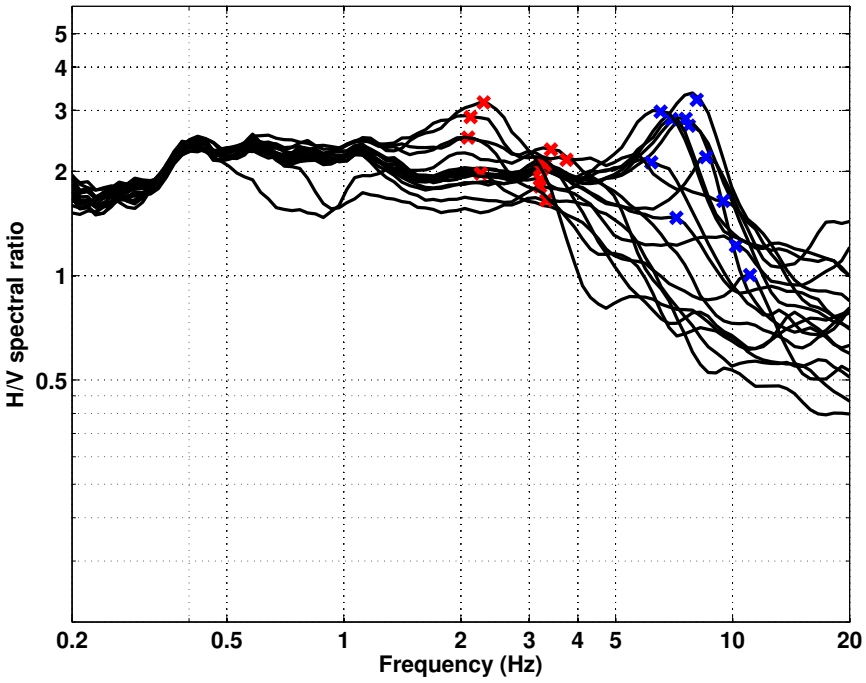

Figure 4: H/V spectral ratios (time-frequency analysis code V. Poggi). The color code of the picked frequency is related to the interpretation (red: Loess layer; blue: weathered Loess layer).

5.3 Polarization analysis

Considering the slope on which the station is installed, a 2D resonance could occur. Therefore, polarization analysis on the array data was performed using the method of Burjánek et al.

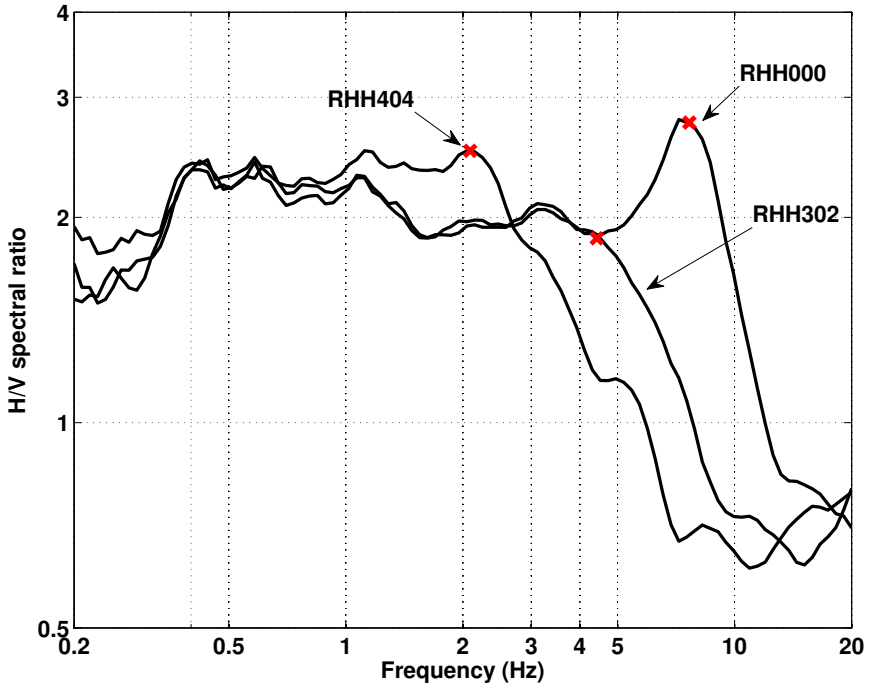

Figure 5: H/V spectral ratios (time-frequency analysis code V. Poggi) for 3 particular points representative of the 3 groups in the description.

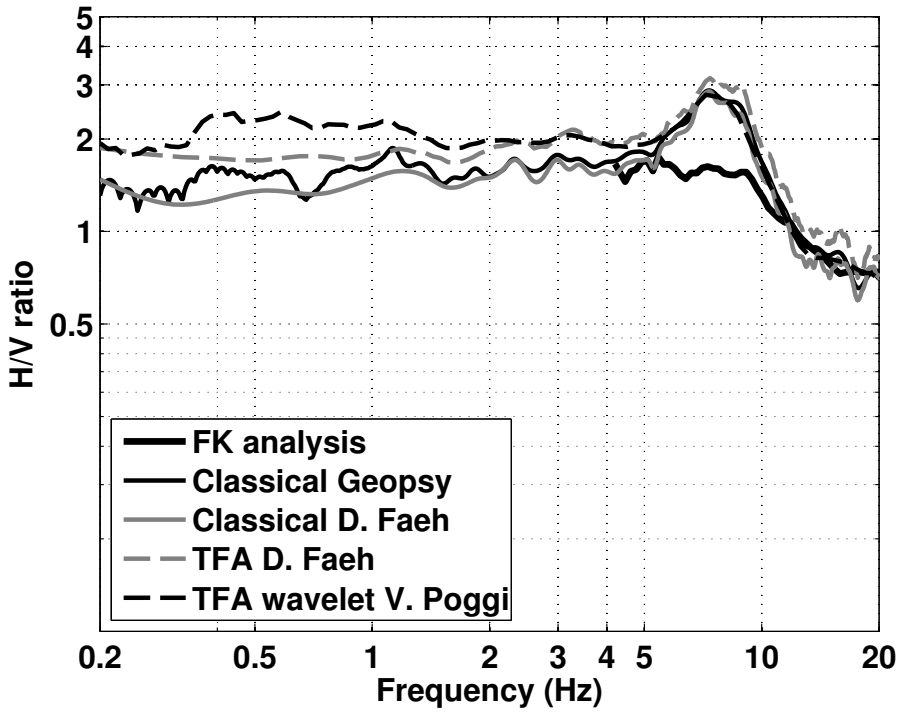

Figure 6: H/V spectral ratios for point RHH000 using the different codes. Classical methods were divided by $\sqrt{2}$.

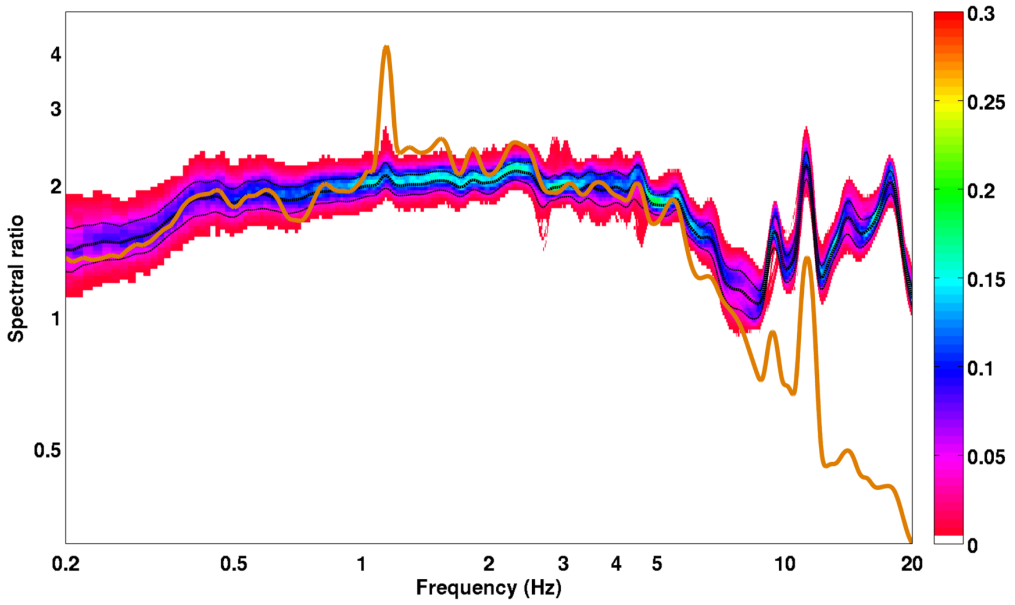

Figure 7: H/V spectral ratios for the accelerometric station SRHH (color fill is the full distribution in time and dashed line are representing mean and standard deviation) compared the long term test station XBA33 (orange thick solid line) located inside the building.

[2010]. All points (Fig. 8) show a polarization in the range 0.5-$3\,\mathrm{Hz}$ perpendicular to the Rhine graben, particularly between 2 and $3\,\mathrm{Hz}$. It is however diffuse and the ellipticity of the ground motion is not particularly low at these frequency. 2D effects are therefore not excluded at this location.

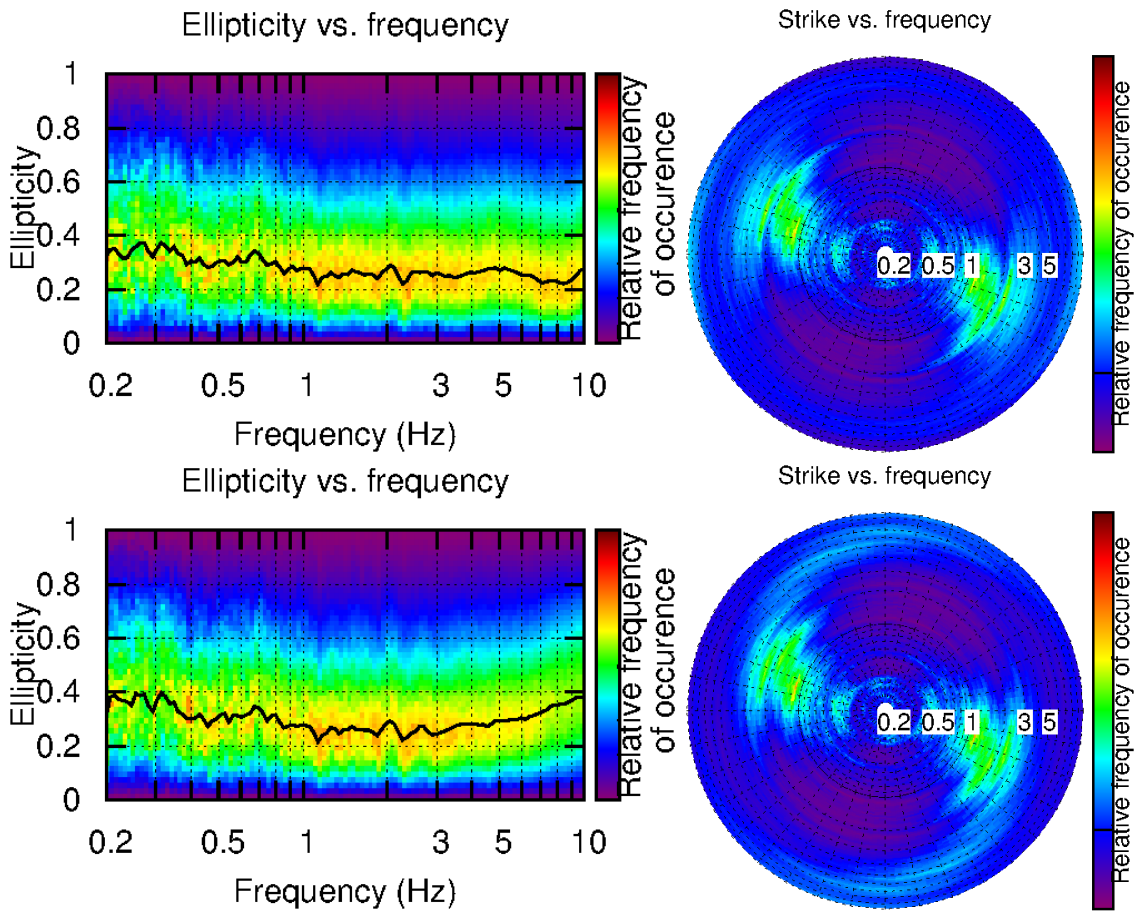

Figure 8: Polarization analysis at point RHH000 (array centre - top) and RHH302 (representative for SRHH - bottom). Left: Ellipticity (A trough in the ellipticity corresponds to polarized motion). Right: Strike of the polarization.

6 Array processing

6.1 Processing methods and parameters

The vertical components of the arrays were processed using the FK and the High-resolution FK analysis [Capon, 1969] using the Geopsy `http://www.geopsy.org` software. Better results were obtained using large time windows (300T). The results of computations of both datasets were too different to be merged and were therefore treated separately.

Moreover, a 3C array analysis [Fäh et al., 2008] was also performed using the array_tool_3C software [Poggi and Fäh, 2010]. It allows to derive Rayleigh and Love modes including the Rayleigh ellipticity. The results of computations of both datasets were too different to be merged and were therefore treated separately.

Method	Set	Freq. band	Win. length	Anti-trig.	Overlap	Grid step	Grid size	# max.
HRFK 1C	1	$1-25\,\mathrm{Hz}$	$300T$	No	50%	0.001	0.6	5
HRFK 1C	2	$1-25\,\mathrm{Hz}$	$300T$	No	50%	0.001	0.6	5
HRFK 3C	1	$1-25\,\mathrm{Hz}$	Wav. 10	No	50%	200	2000	5
			Tap. 0.2			m/s	m/s	
HRFK 3C	2	$1-25\,\mathrm{Hz}$	Wav. 10	No	50%	200	2000	5
			Tap. 0.2			m/s	m/s	

Table 5: Methods and parameters used for the array processing.

6.2 Obtained dispersion curves

As it could be expected from the H/V analysis, a large difference between the first and the second configuration is found in the FK analysis. In all cases only fundamental modes could be picked. For the first configuration, the fundamental Rayleigh mode is clearer in the 1C analysis compared to the 3C analysis although the match is acceptable. It can be picked with confidence between 6 and $22\,\mathrm{Hz}$, with velocities from 1270 to $370\,\mathrm{m/s}$. The picking on Fig. 9 goes beyond the array resolution limit and should be shortened for inversion purposes. The fundamental Love mode could be picked between $5.4\,\mathrm{Hz}$ and $14.6\,\mathrm{Hz}$ (Fig. 10). The velocities are ranging from $860\,\mathrm{m/s}$ at $5.4\,\mathrm{Hz}$ down to $270\,\mathrm{m/s}$ at $14.6\,\mathrm{Hz}$. For the second configuration, fundamental Rayleigh mode is found from both 1C and 3C analysis between 3 and $6\,\mathrm{Hz}$ and fundamental Love mode between 2 and $8\,\mathrm{Hz}$.

All picked curves are presented together on Fig. 11. The curves from the second configuration are shifted to the left with respect to the first configuration, indicating that it samples an area with deeper sedimentary cover.

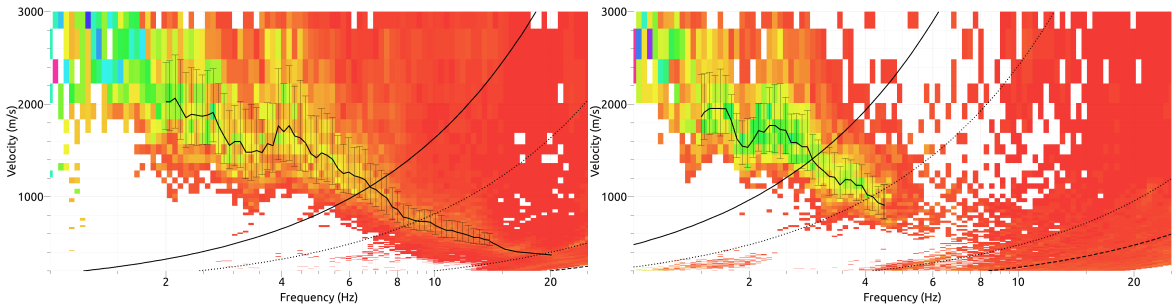

Figure 9: Dispersion curves obtained from the 1C array analyses (left: first configuration; right: second configuration).

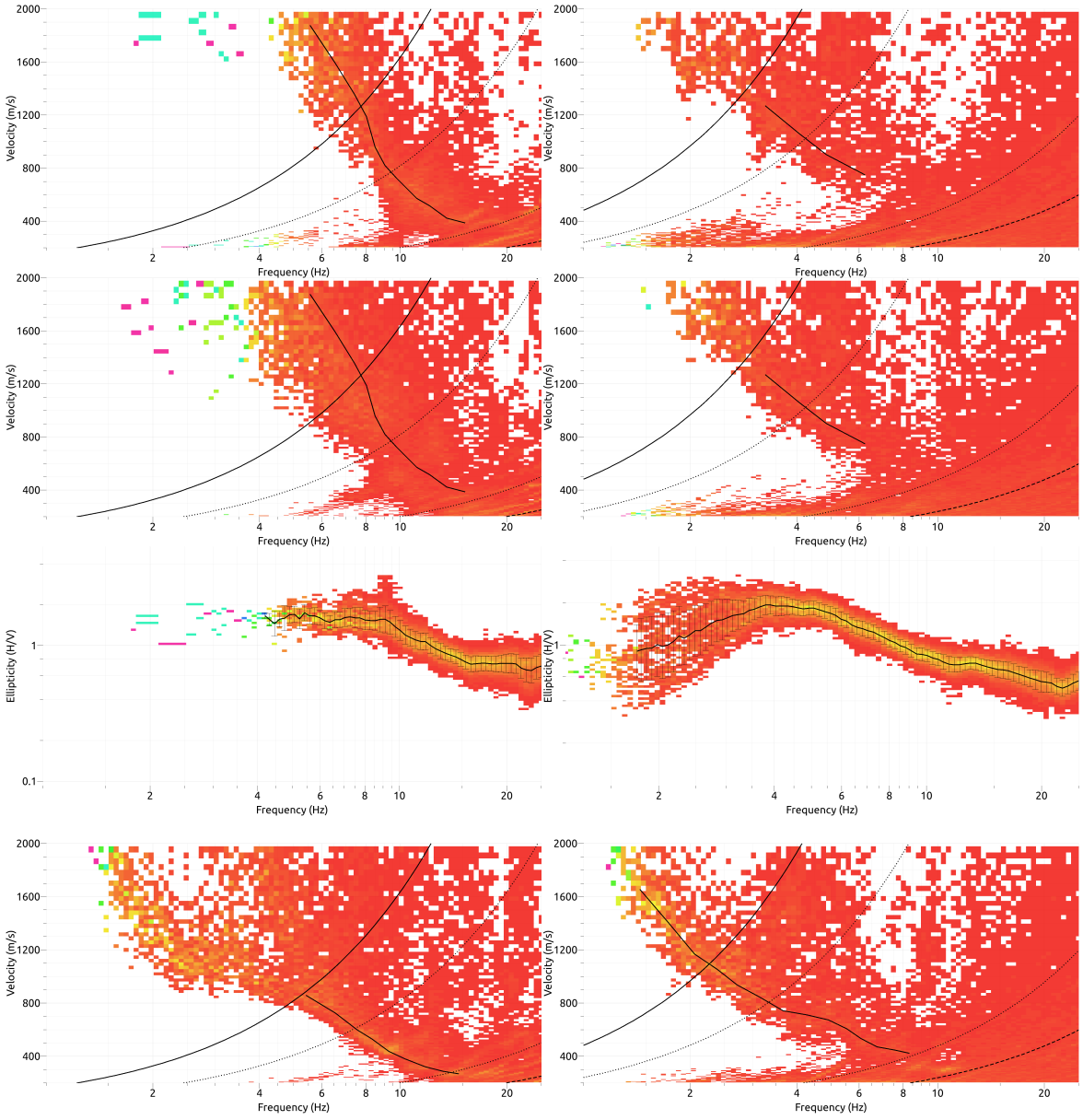

Figure 10: Dispersion curves and ellipticity obtained from the 3C array analyses (from top to bottom: vertical, radial, ellipticity and transverse components; left: first configuration; right: second configuration).

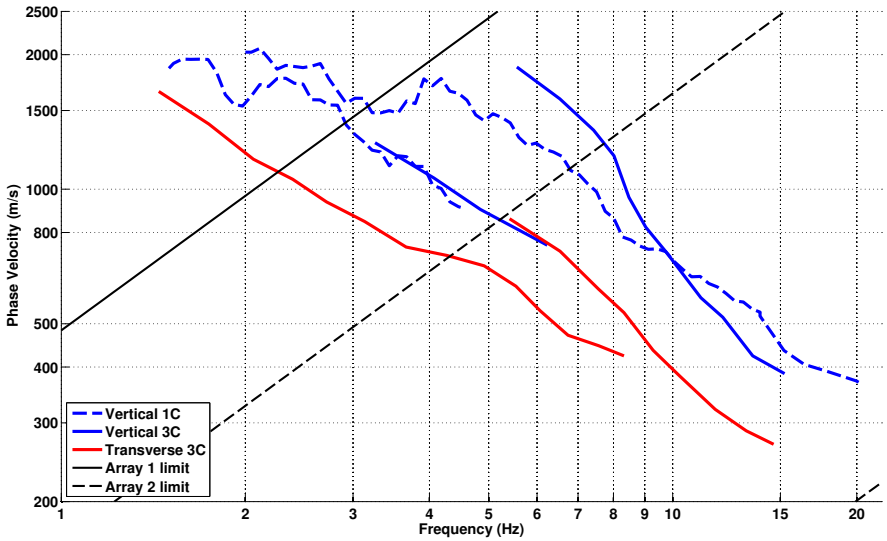

Figure 11: Picked dispersion curves from 1C and 3C FK methods.

7 Inversion and interpretation

7.1 Inversion

For the inversion, Rayleigh and Love fundamental modes dispersion curves, as well as the ellipticity curve and the fundamental frequency were used as simultaneous targets without standard deviation to avoid different weighting. Two separated inversions were conducted for the two array configurations: dataset 1 is representative of point RHH000, close to the station SRHH, whereas dataset 2 is representative for point RHH404, at the top of the hill. The fundamental frequency was set at 3.2 and $2.1\,\mathrm{Hz}$ for these two inversions, respectively. A weight of 0.2 was assigned to the ellipticity peak and 0.05 (very low) to the ellipticity curve. All curves were resampled using 50 points between 1 and $21\,\mathrm{Hz}$ in log scale.

The inversion was performed using the Improved Neighborhood Algorithm (NA) Wathelet [2008] implemented in the Dinver software. In this algorithm, the tuning parameters are the following: Ns_0 is the number of starting models, randomly distributed in the parameter space, Nr is the the number of best cells considered around these Ns_0 models, Ns is the number of new cells generated in the neighborhood of the Nr cells (Ns/Nr per cell) and It_{max} is the number of iteration of this process. The process ends with $Ns_0 + Nr * \frac{Ns}{Nr} * It_{max}$ models. The used parameters are detailed in Tab. 6.

It_{max}	Ns_0	Ns	Nr
500	10000	100	100

Table 6: Tuning parameters of Neighborhood Algorithm.

According to geology (section 2), Quaternary sediments of 10 to $30\,\mathrm{m}$ with low velocities are expected on top of Mesozoic rock. Therefore, the velocity is expected to increase with depth and no low velocity zone was allowed. Dataset 2 refers to a zone located $10\,\mathrm{m}$ above dataset 1 in elevation. The Poisson ratio was inverted in each layer in the range 0.2-0.4. The density was assumed to be 1800 in the sediments and $2500\,\mathrm{kg/m^3}$ in the rock. Inversions with free layer depths as well as fixed layer depths were performed. 3 layers are enough to explain most of the targets (dispersion and ellipticity), but more layers are used to smooth the obtained results and better explore the parameter space. 5 independent runs of 5 different parametrization schemes (2 and 3 layers over a half space and 10 layers with fixed depth) were performed. For further elaborations, the best models of these 25 runs were selected (Fig. 18).

A single layer of sediments over the bedrock cannot explain the observed dispersion and ellipticity. An intermediate layer of weathered rock is needed. The inversions indicate in both datasets a layer of sediments of 10 to $15\,\mathrm{m}$ depth with a velocity of 150 to $500\,\mathrm{m/s}$. For dataset 1, all parametrizations lead to profiles with a clear velocity contrast with a layer at 1000 to $1300\,\mathrm{m/s}$, extending down to 90 to $120\,\mathrm{m}$ depth. Below the bedrock is found with a velocity of about $2000\,\mathrm{m/s}$. For dataset 2, the fixed layers depth parametrization lead to solutions without clear contrast between sediments and rock but a gradient in the rock is found with velocities from 600 to $1300\,\mathrm{m/s}$. However, free layer depth solutions are the same as for dataset 1, simply with 10 more meters in the top layer. The interface with the bedrock is found deeper at 150 to $200\,\mathrm{m}$ depth, also with a velocity of about $2000\,\mathrm{m/s}$. This deeper interface is not corresponding

to the known geological setting (considering the normal faults, it should be shallower or equal) and may be representing the uncertainty of the inversion. The inversion of dataset 2 is therefore to be taken with care.

When comparing to the target curves (Fig. 13 and Fig. 14), the Rayleigh and Love fundamental modes are well represented. Though the weight on the ellipticity curve is very low, the ellipticity of the inverted models makes sense compared to the observations.

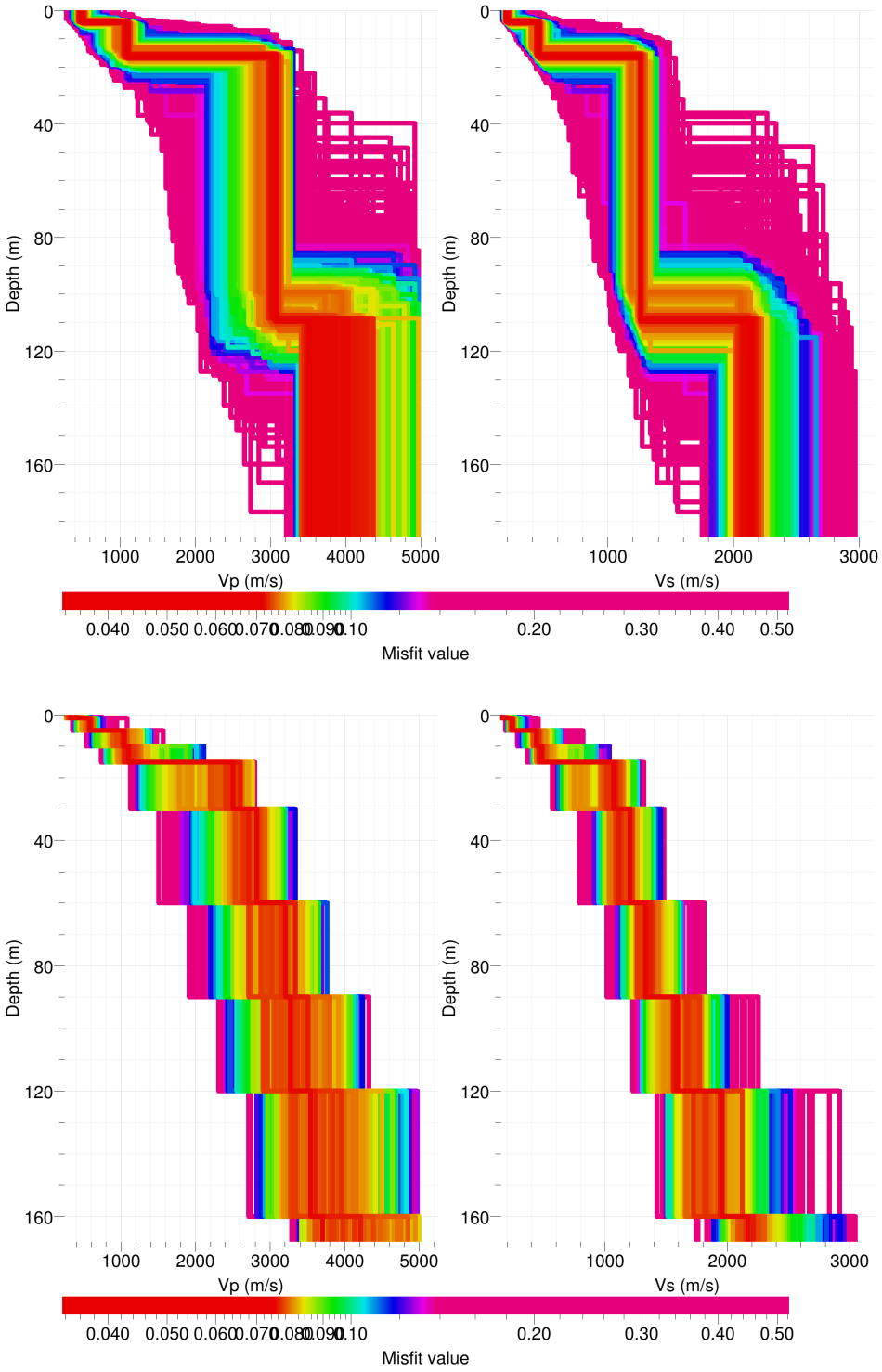

Figure 12: Dataset 1: Inverted ground profiles in terms of V_p and V_s; top: free layer depth strategy; bottom: fixed layer depth strategy.

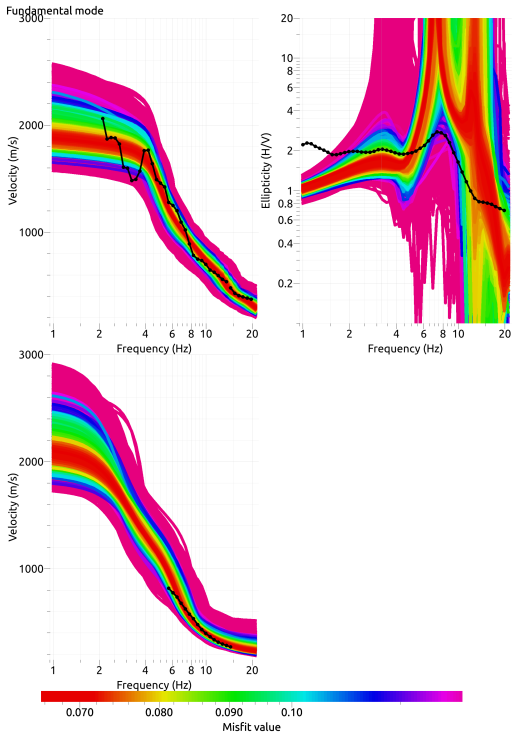

Figure 13: Dataset 1: Comparison between inverted models and measured Rayleigh and Love modes and corresponding ellipticity, free layer depth strategy.

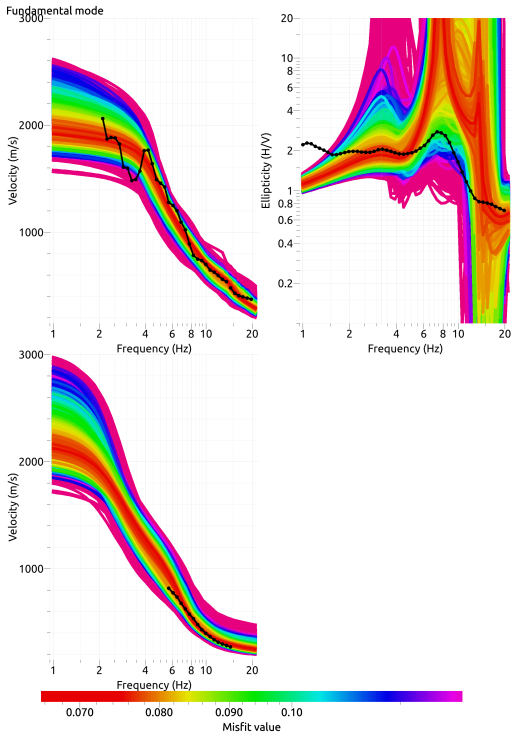

Figure 14: Dataset 1: Comparison between inverted models and measured Rayleigh and Love modes and corresponding ellipticity, fixed layer depth strategy.

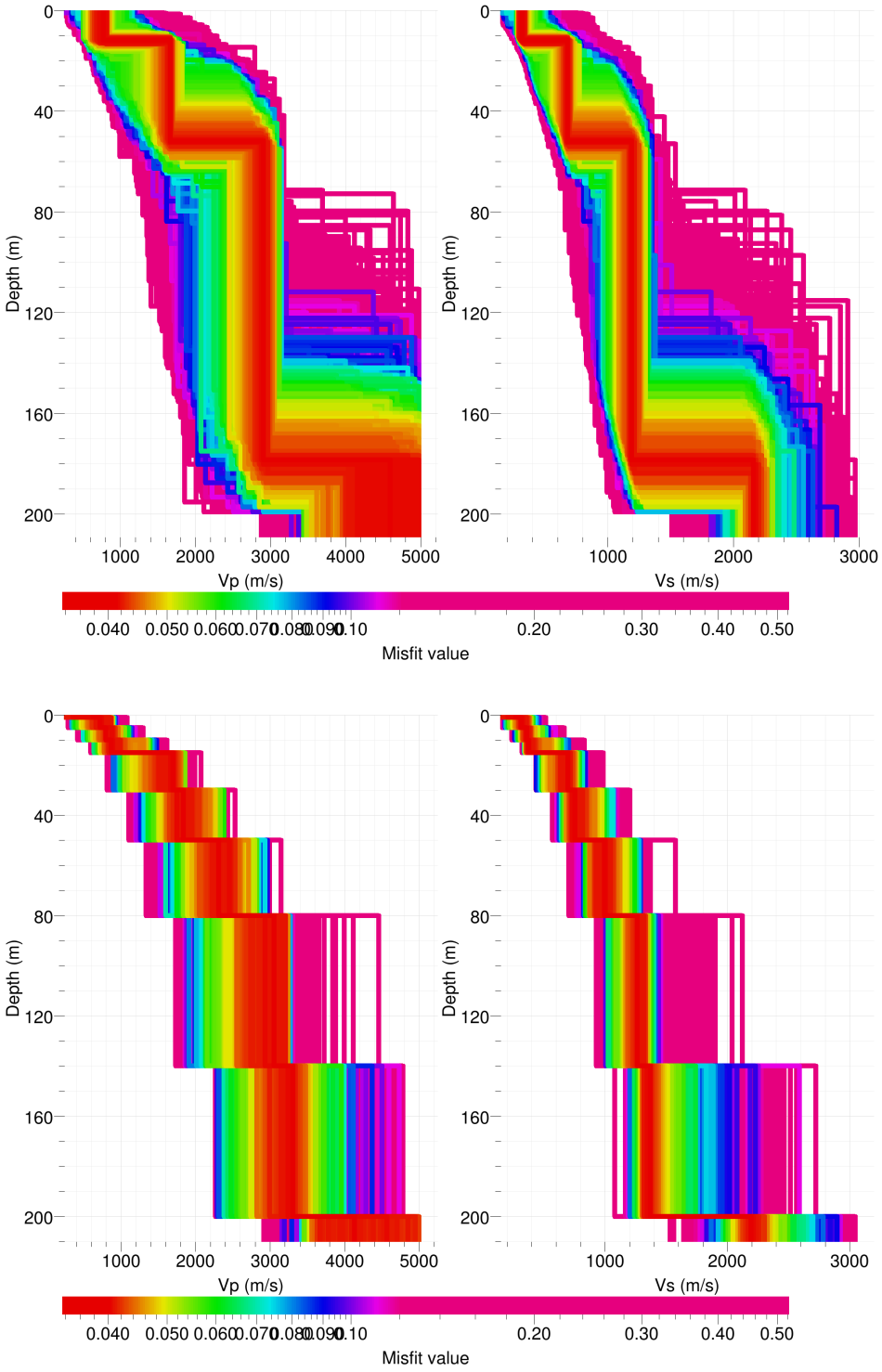

Figure 15: Dataset 2: Inverted ground profiles in terms of V_p and V_s; top: free layer depth strategy; bottom: fixed layer depth strategy.

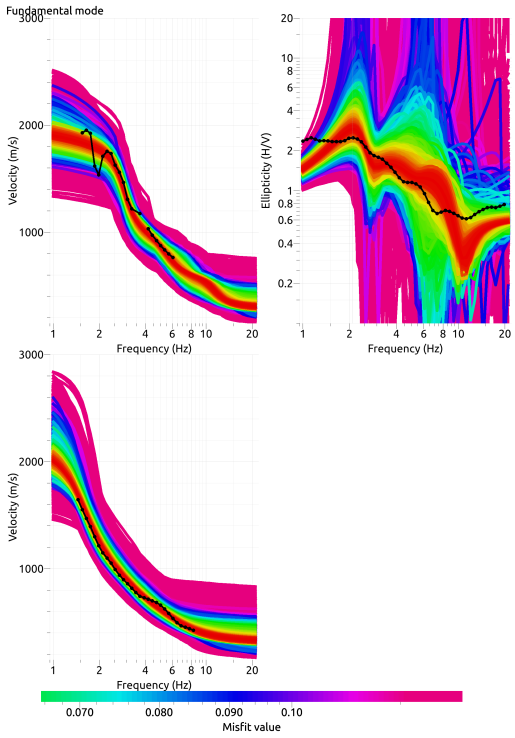

Figure 16: Dataset 2: Comparison between inverted models and measured Rayleigh and Love modes and corresponding ellipticity, free layer depth strategy.

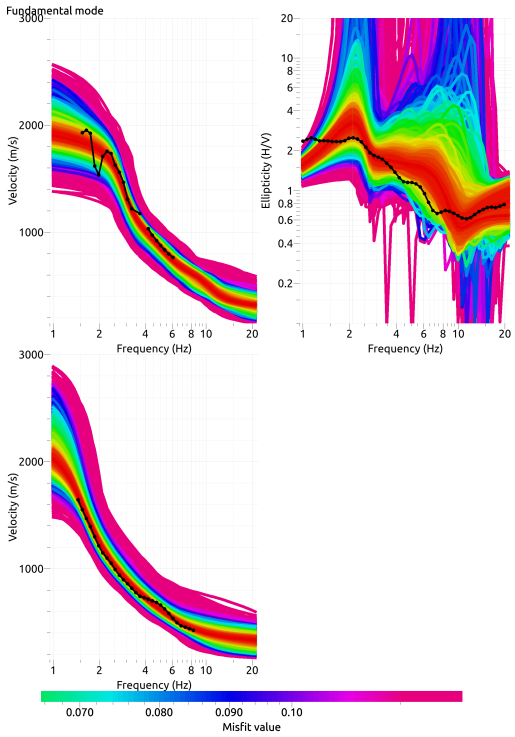

Figure 17: Dataset 2: Comparison between inverted models and measured Rayleigh and Love modes and corresponding ellipticity, fixed layer depth strategy.

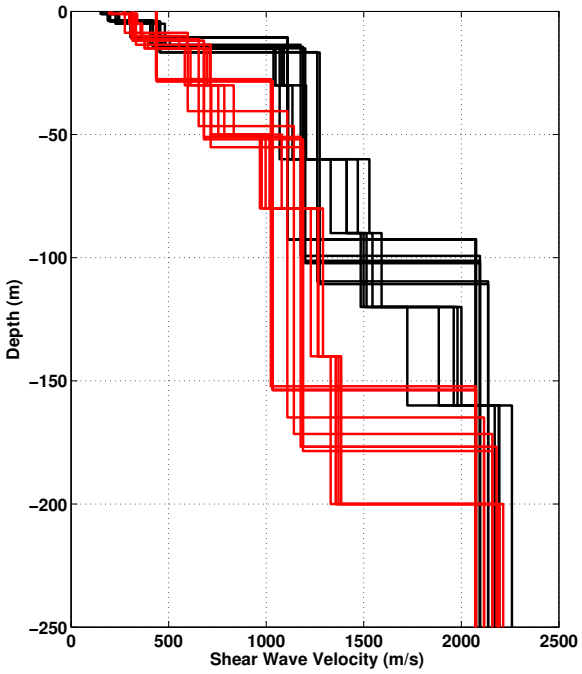

Figure 18: V_s ground profiles for the selected 25 best models (dataset 1: black; dataset 2: red).

7.2 Travel time average velocities and ground type

The distribution of the travel time average velocities at different depths was computed from the selected models. The uncertainty, computed as the standard deviation of the distribution of travel time average velocities for the considered models, is also provided, but its meaning is doubtful. $V_{s,30}$ is found to be $534\,\mathrm{m/s}$. The site can be classified as ground type E in the Eurocode 8 [CEN, 2004] and the SIA261 [SIA, 2003]: the first $10-15\,\mathrm{m}$ at $150-350\,\mathrm{m/s}$ are lying on rock at $1000\,\mathrm{m/s}$.

7.3 SH transfer function and quarter-wavelength velocity

The quarter-wavelength velocity approach [Joyner et al., 1981] provides, for a given frequency, the average velocity at a depth corresponding to 1/4 of the wavelength of interest. It is useful to identify the frequency limits of the experimental data (minimum frequency in dispersion curves and ellipticity peak at $3\,\mathrm{Hz}$ here). The results using this proxy show that the data constrain the profiles down to $65\,\mathrm{m}$ (Fig. 19). Moreover, the quarter wavelength impedance-contrast introduced by Poggi et al. [2012a] is also displayed in the figure. It corresponds to the ratio between two quarter-wavelength average velocities, respectively from the top and the bottom part of the velocity profile, at a given frequency [Poggi et al., 2012a]. It shows a trough (inverse shows a peak) at the resonance frequency.
Moreover, the theoretical SH-wave transfer function for vertical propagation [Roesset, 1970]

	Mean (m/s)	**Uncertainty (m/s)**
$V_{s,5}$	248	44
$V_{s,10}$	297	8
$V_{s,20}$	423	32
$V_{s,30}$	534	32
$V_{s,40}$	616	30
$V_{s,50}$	679	28
$V_{s,100}$	881	15
$V_{s,150}$	1075	22
$V_{s,200}$	1225	19

Table 7: Travel time averages at different depths from the inverted models. Uncertainty is given as one standard deviation from the selected profiles.

is computed from the inverted profiles. It is compared to the quarter-wavelength amplification [Joyner et al., 1981] that however cannot take resonances into account (Fig. 20). In this case, the models are predicting a small peak at about $3\,\mathrm{Hz}$ due to the contrast within the rock and a major peak around $6-7\,\mathrm{Hz}$ due to the sedimentary cover. The ESM amplification function [Edwards et al., 2013] is showing on Fig. 21 that these two peaks exist and the amplitude is reproduced. However, it also shows more complexity with more peaks at lower and higher frequencies.

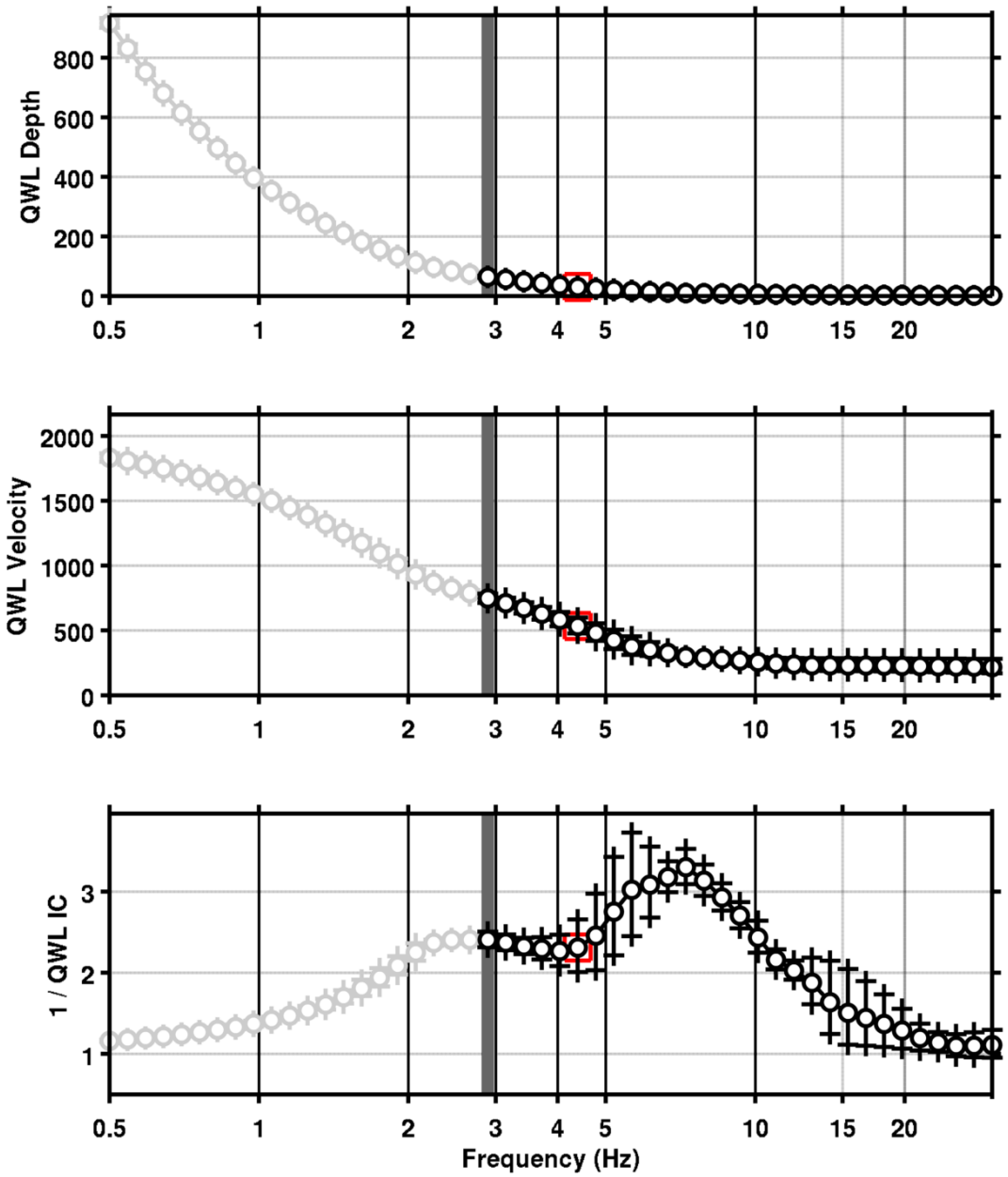

Figure 19: Quarter wavelength velocity representation of the velocity profile (top: depth, centre: velocity, bottom: inverse of the impedance contrast). Black curve is constrained by the dispersion curves, light grey is not constrained by the data. Red square is corresponding to $V_{s,30}$.

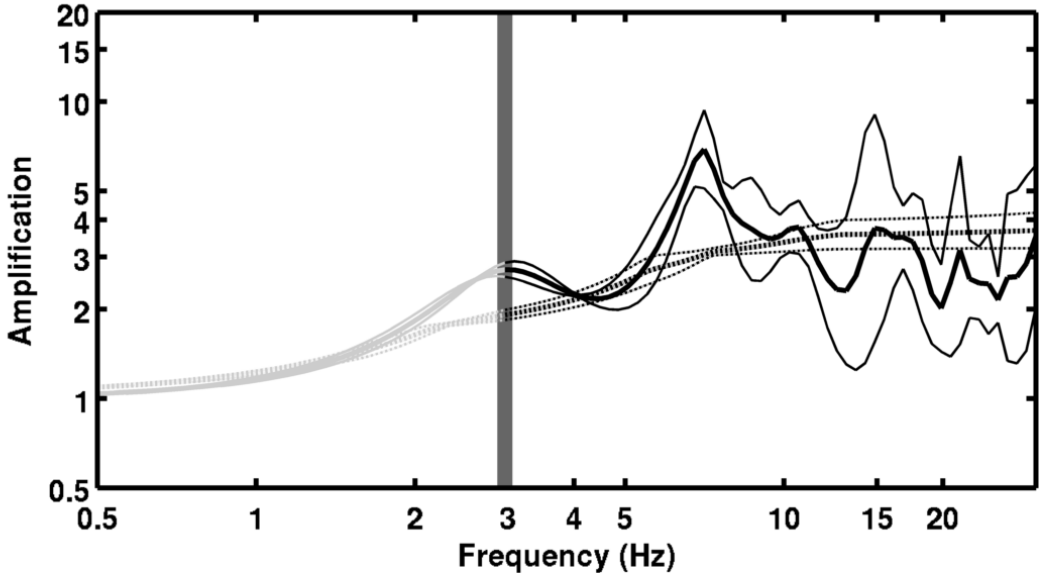

Figure 20: Theoretical SH transfer function (solid line) and quarter wavelength impedance contrast (dashed line) with their standard deviation. Significance of the greyshades is detailed in Fig. 19.

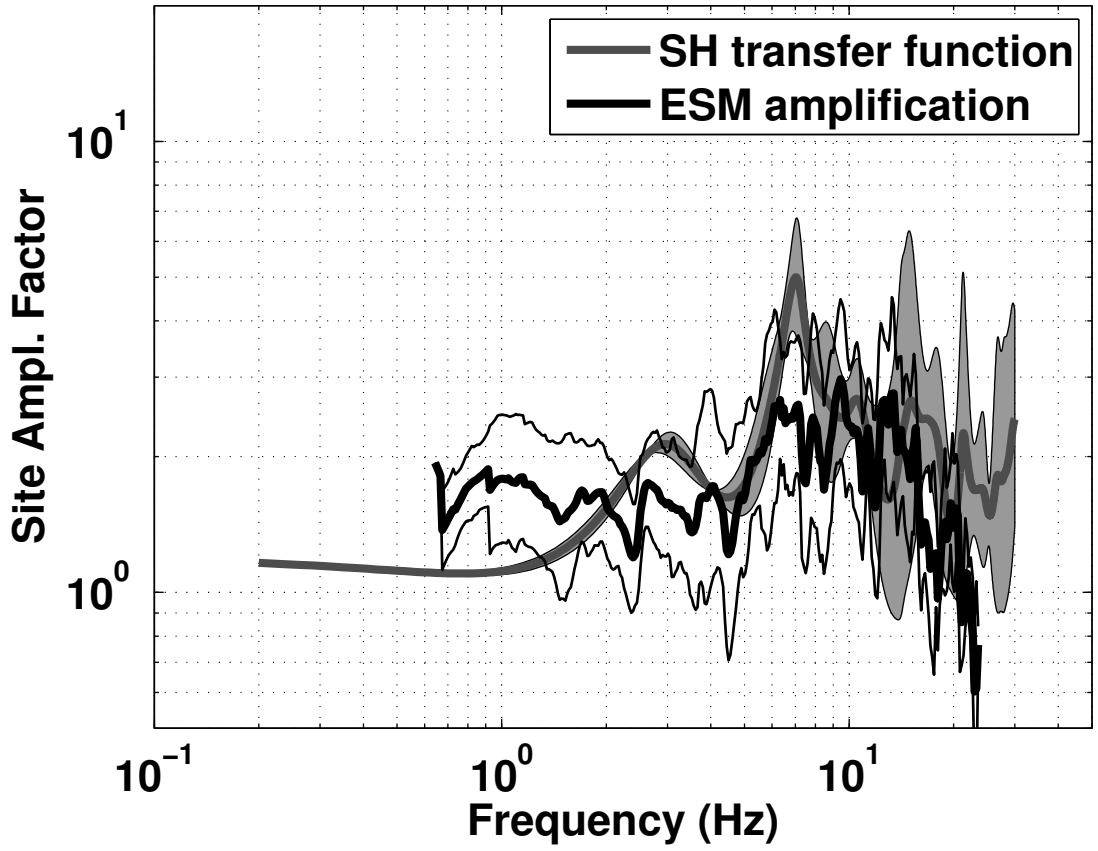

Figure 21: Theoretical SH transfer function (grey line with uncertainty) and Empirical Spectral Modeling Amplification function (black lines) with its standard deviation. Both functions are referenced on the Swiss rock reference model.

8 Conclusions

The array measurements presented in this study were successful in deriving a velocity model for the site of the SRHH station, although the site shows heavy lateral heterogeneity, including normal faulting. We found a layer of sediments made of Loess of 10 to $15\,\mathrm{m}$ depth with a velocity of 150 to $500\,\mathrm{m/s}$. The velocity contrast is clear with a layer at 1000 to $1300\,\mathrm{m/s}$, extending down to 90 to $120\,\mathrm{m}$ depth. Below the bedrock is found with a velocity of about $2000\,\mathrm{m/s}$. The sedimentary layer is creating a resonance peak around $6-7\,\mathrm{Hz}$, whereas the contrast in the rock is creating a small peak at about $3\,\mathrm{Hz}$, corresponding to the "fundamental" peak from the H/V ratios. These peak are effectively seen in the empirical amplification function.
$V_{s,30}$ is $534\,\mathrm{m/s}$ and the ground type in the Eurocode 8 [CEN, 2004] and the SIA261 [SIA, 2003] is E due to the shallow Loess layer lying on rock. The theoretical 1D SH transfer function and impedance contrast of the quarter-wavelength velocity computed from the inverted profiles show a large amplification at high frequency.

Acknowledgements

The authors thank Ashraf Adli for his help during these measurements.

References

Sylvette Bonnefoy-Claudet, Fabrice Cotton, and Pierre-Yves Bard. The nature of noise wavefield and its applications for site effects studies. *Earth-Science Reviews*, 79(3-4): 205–227, December 2006. ISSN 00128252. doi: 10.1016/j.earscirev.2006.07.004. URL http://linkinghub.elsevier.com/retrieve/pii/S0012825206001012.

Jan Burjánek, Gabriela Gassner-Stamm, Valerio Poggi, Jeffrey R. Moore, and Donat Fäh. Ambient vibration analysis of an unstable mountain slope. *Geophysical Journal International*, 180(2):820–828, February 2010. ISSN 0956540X. doi: 10.1111/j.1365-246X.2009.04451.x. URL http://gji.oxfordjournals.org/cgi/doi/10.1111/j.1365-246X.2009.04451.xhttp://doi.wiley.com/10.1111/j.1365-246X.2009.04451.x.

J. Capon. High-Resolution Frequency-Wavenumber Spectrum Analysis. *Proceedings of the IEEE*, 57(8):1408–1418, 1969. ISSN 0018-9219. doi: 10.1109/PROC.1969.7278. URL http://ieeexplore.ieee.org/lpdocs/epic03/wrapper.htm?arnumber=1449208.

CEN. *Eurocode 8: Design of structures for earthquake resistance - Part 1: General rules, seismic actions and rules for buildings*. European Committee for Standardization, en 1998-1: edition, 2004.

Benjamin Edwards, Clotaire Michel, Valerio Poggi, and Donat Fäh. Determination of Site Amplification from Regional Seismicity : Application to the Swiss National Seismic Networks. *Seismological Research Letters*, 84(4), 2013. doi: 10.1785/0220120176.

Donat Fäh and Peter Huggenberger. INTERREG III Projekt: Erdbebenmikrozonierung am südlichen Oberrhein. Zusammenfassung. Technical report, Eidgenössische Technische Hochschule Zürich (ETHZ), 2006.

Donat Fäh, Fortunat Kind, and Domenico Giardini. A theoretical investigation of average H / V ratios. *Geophysical Journal International*, 145:535–549, 2001.

Donat Fäh, Gabriela Stamm, and Hans-Balder Havenith. Analysis of three-component ambient vibration array measurements. *Geophysical Journal International*, 172(1):199–213, January 2008. ISSN 0956540X. doi: 10.1111/j.1365-246X.2007.03625.x. URL http://doi.wiley.com/10.1111/j.1365-246X.2007.03625.xhttp://gji.oxfordjournals.org/cgi/doi/10.1111/j.1365-246X.2007.03625.x.

Donat Fäh, Marc Wathelet, Miriam Kristekova, Hans-Balder Havenith, Brigitte Endrun, Gabriela Stamm, Valerio Poggi, Jan Burjánek, and Cécile Cornou. Using Ellipticity Information for Site Characterisation. Technical report, NERIES JRA4 Task B2, 2009.

William B. Joyner, Richard E. Warrick, and Thomas E. Fumal. The effect of Quaternary alluvium on strong ground motion in the Coyote Lake, California, earthquake of 1979. *Bulletin of the Seismological Society of America*, 71(4):1333–1349, 1981.

Katsuaki Konno and Tatsuo Ohmachi. Ground-Motion Characteristics Estimated from Spectral Ratio between Horizontal and Vertical Components of Microtremor. *Bulletin of the Seismological Society of America*, 88(1):228–241, 1998.

Valerio Poggi and Donat Fäh. Estimating Rayleigh wave particle motion from three-component array analysis of ambient vibrations. *Geophysical Journal International*, 180(1):251–267, January 2010. ISSN 0956540X. doi: 10.1111/j.1365-246X.2009.04402.x. URL http://doi.wiley.com/10.1111/j.1365-246X.2009.04402.x.

Valerio Poggi, Benjamin Edwards, and Donat Fäh. Characterizing the Vertical-to-Horizontal Ratio of Ground Motion at Soft-Sediment Sites. *Bulletin of the Seismological Society of America*, 102(6):2741–2756, December 2012a. ISSN 0037-1106. doi: 10.1785/0120120039. URL http://www.bssaonline.org/cgi/doi/10.1785/0120120039.

Valerio Poggi, Donat Fäh, Jan Burjánek, and Domenico Giardini. The use of Rayleigh-wave ellipticity for site-specific hazard assessment and microzonation: application to the city of Lucerne, Switzerland. *Geophysical Journal International*, 188(3):1154–1172, March 2012b. ISSN 0956540X. doi: 10.1111/j.1365-246X.2011.05305.x. URL http://doi.wiley.com/10.1111/j.1365-246X.2011.05305.xhttp://gji.oxfordjournals.org/cgi/doi/10.1111/j.1365-246X.2011.05305.x.

J.M. Roesset. Fundamentals of soil amplification. In R. J. Hansen, editor, *Seismic Design for Nuclear Power Plants*, pages 183–244. M.I.T. Press, Cambridge, Mass., 1970. ISBN 978-0-262-08041-5. URL http://mitpress.mit.edu/catalog/item/default.asp?ttype=2&tid=5998.

SIA. *SIA 261 Actions sur les structures porteuses*. Société suisse des ingénieurs et des architectes, Zürich, sia 261:20 edition, 2003.

Hirotoshi Uebayashi, Hidenori Kawabe, and Katsuhiro Kamae. Reproduction of microseism H/V spectral features using a three-dimensional complex topographical model of the sediment-bedrock interface in the Osaka sedimentary basin. *Geophysical Journal International*, 189(2):1060–1074, May 2012. ISSN 0956540X. doi: 10.1111/j.1365-246X.2012.05408.x. URL http://gji.oxfordjournals.org/cgi/doi/10.1111/j.1365-246X.2012.05408.x.

Marc Wathelet. An improved neighborhood algorithm: Parameter conditions and dynamic scaling. *Geophysical Research Letters*, 35(9):1–5, May 2008. ISSN 0094-8276. doi: 10.1029/2008GL033256. URL http://www.agu.org/pubs/crossref/2008/2008GL033256.shtml.